ACS Energy LETTERS

Cite This: ACS Energy Lett. 2018, 3, 2931−2939

http://pubs.acs.org/journal/aelccp

LETTER

Improving Charge Carrier Delocalization in Perovskite Quantum Dots by Surface Passivation with Conductive Aromatic Ligands

Evan T. Vickers,[†] Thomas A. Graham,[†] Ashraful H. Chowdhury,[‡] Behzad Bahrami,[‡] Benjamin W. Dreskin,[†] Sarah Lindley,[†] Sara Bonabi Naghadeh,[†] Qiquan Qiao,[‡] and Jin Z. Zhang*[,†]

[†]Department of Chemistry and Biochemistry, University of California, Santa Cruz, California 95064, United States

[‡]Center for Advanced Photovoltaics and Sustainable Energy, Department of Electrical Engineering and Computer Science, South Dakota State University, Brookings, South Dakota, 57007, United States

Supporting Information

ABSTRACT: Long-chain saturated hydrocarbons and alkoxysilanes are ligands that are commonly used to passivate perovskite quantum dots (PQDs) to enhance their stability and optical properties. However, the insulating nature of these capping ligands creates an electronic energy barrier and impedes interparticle electronic coupling, thereby limiting device applications. One strategy to solve this problem is the use of short conductive aromatic ligands that allow delocalization of the electronic wave function from the PQDs, which, in turn, facilitates charge transport between PQDs by lowering the energy barrier. This is demonstrated with methylammonium lead bromide ($MAPbBr_3$) QDs prepared using benzylamine (BZA) and benzoic acid (BA) capping ligands. Optimized BZA-BA-$MAPbBr_3$ QDs are highly stable and show very high photoluminescence (PL) quantum yield (QY) (86%). More importantly, the BZA-BA-$MAPbBr_3$ QD film exhibits higher conductivity and carrier lifetime and more efficient charge extraction compared to PQDs with insulating ligands, as indicated by electrochemical measurements and transient photocurrent and photovoltage spectroscopy.

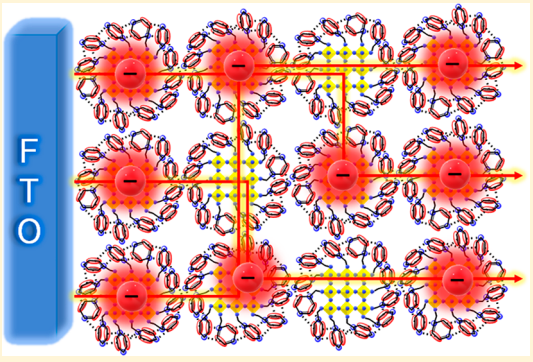

Semiconductor quantum dots (QDs) are highly valued materials for optoelectronic applications because of their novel optical and electronic properties.[1−9] This is partly due to strong quantum confinement in the nanometer size regime.[10−12] In addition, their low-cost solution processing is a major advantage for device fabrication. Semiconductor QDs based on organometal halide perovskites with the formula $APbX_3$ (A = methylammonium (MA) or cesium, X = Cl, Br, I) have recently shown great promise for light-emitting diode (LED) and photovoltaic (PV) applications. However, one of the most important challenges hindering their practical use is instability in the presence of oxygen, moisture, temperature, and UV light.[13−22]

One approach for stabilizing the perovskite quantum dots (PQDs) is to use molecular ligands to passivate the surface, such as long alkyl chains and alkoxysilanes, that enhance optical properties and improve stability because of their hydrophobicity and steric hindrance toward infiltrating water and oxygen molecules.[8,9,17,20−29] However, these capping ligands are insulators and present energy barriers that obstruct charge carrier transport within the PQD solids. This not only inhibits charge transport at the interface of PQDs and conductive contact layers but also impedes PQD electronic coupling in the solid film. In consequence, it is challenging to fabricate PQD films with enough light absorption and sufficient charge transport to compete with unprotected perovskite polycrystalline films or inorganic capped QDs.[30−35] A major focus toward increasing charge transport and interdot electronic coupling is tuning the length of the capping ligands.[36−40] This has led to the use of short ligands that contain multiple functional groups to passivate diverse defect sites and decrease the distance between QDs toward increasing charge transport in molecular electronic junctions.[41−47] In addition, bifunctional aromatic capping ligands have been used as an effective tool for linking a conductive contact film with QDs at their interfacial region as well as strengthening the coupling between QDs in the solid film.[36,37,46,48−55] Furthermore, surface passivation of colloidal PQDs with conjugated aromatic capping ligands were previously reported; however, the conjugated ligands were

Received: September 17, 2018
Accepted: November 12, 2018
Published: November 12, 2018

DOI: 10.1021/acsenergylett.8b01754
ACS Energy Lett. 2018, 3, 2931−2939

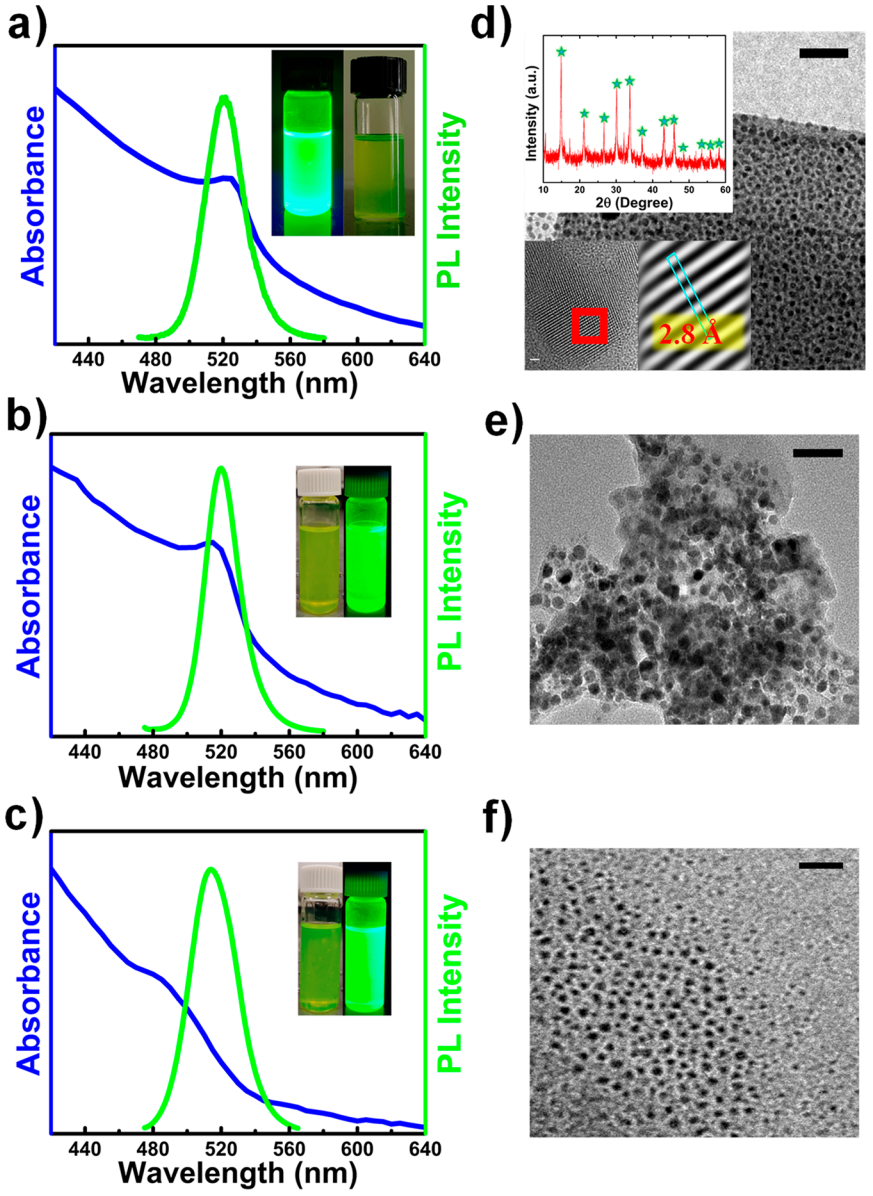

Figure 1. UV−vis absorption and PL spectra of (a) BZA-BA-MAPbBr$_3$, (b) APTES-OA-MAPbBr$_3$, and (c) OCTA-OA-MAPbBr$_3$ QDs. Insets are digital photographs of the respective QD solution. (d) TEM image of BZA-BA-MAPbBr$_3$ QDs (scale bar 50 nm). The lower left inset is HRTEM image with lattice spacing (scale bar 1 nm), and the upper left inset is XRD pattern with symbols assigned to the cubic phase. TEM images of (e) APTES-OA-MAPbBr$_3$ (scale bar 50 nm) and (f) OCTA-OA-MAPbBr$_3$ QDs (scale bar 20 nm).

used in conjunction with oleic acid.[56] Therefore, surface passivation of colloidal PQDs with exclusively conjugated capping ligands has yet to be established.

The problem of concurrently preventing moisture penetration and improving charge transport can be solved by introducing hydrophobic capping ligands with conductive properties. This enables water-resistivity as well as lower charge-resistivity in a PQD solid. Prospective capping ligands with hydrophobicity and conductive properties include aromatic, alkene, and alkyne compounds with an unhindered positive or negative terminal ion that will interact strongly with the ions of the perovskite lattice. Aromatic compounds are especially promising because of the special stability from its resonance delocalization of π-electrons. Coupled with stability, addition of electron-donating and -withdrawing groups to the aromatic system enables fine-tuning of its electronic structure and energy level alignment, which is essential for solar cell and LED device fabrication. Benzylamine has been previously used to passivate crystalline perovskite for solar cells.[57,58] Wang et al. surface-passivated formamidinium lead iodide (FAPbI$_3$) films with aniline, benzylamine, and phenethylamine and observed that benzylamine has the optimal steric arrangement in conjunction with the perovskite surface to block moisture and enhance stability. Moreover, Zhou et al. observed highly efficient surface passivation of defect regions that suppressed thermal photoinduced degradation.

Herein, we introduce for the first time colloidal MAPbBr$_3$ QDs with only short conductive aromatic capping ligands. MAPbBr$_3$ QDs were successfully synthesized using benzylamine (BZA) and benzoic acid (BA) capping ligands. In the optimal synthesis, BZA-BA-MAPbBr$_3$ QDs are observed to have a high photoluminescence quantum yield (PLQY) of 86 ± 5% (vs fluorescein, 95%), indicative of a well-passivated surface. Moreover, transient photovoltage (TPV) and transient

DOI: 10.1021/acsenergylett.8b01754
ACS Energy Lett. 2018, 3, 2931−2939

photocurrent (TPC) spectroscopy as well as electroanalytical measurements, such as electrochemical impedance spectroscopy (EIS) and cyclic voltammetry (CV), have provided evidence that BZA-BA-$MAPbBr_3$ QDs in solid film possess highly desirable electrical properties compared to PQDs passivated with the commonly used insulating long alkyl chains and alkoxysilanes.

Methylammonium lead bromide quantum dots ($MAPbBr_3$) QDs were synthesized following a previously reported procedure.[20,59] A precursor solution consisting of $PbBr_2$, MABr, benzylamine (BZA), and benzoic acid (BA) dissolved in *N*,*N*-dimethylformamide (DMF) was injected into toluene. The colloidal BZA-BA-$MAPbBr_3$ QD solution was then purified using centrifugation and cotton-plug filtration. Optimization of PQDs with the highest quantum yield (QY) was determined by adjusting BZA and BA concentrations discretely. Detailed information about the synthesis is in the Supporting Information. The highest relative QY obtained from BZA-BA-$MAPbBr_3$ QDs is 86% (vs fluorescein, 95%). The ultraviolet−visible (UV−vis) absorption and photoluminescence (PL) spectra of BZA-BA-$MAPbBr_3$ QDs are displayed in Figure 1a. As shown, the BZA-BA-$MAPbBr_3$ QDs exhibited a strong absorption peak at 520 nm and slight Stokes shift in PL at 525 nm. The full-width half-maximum (fwhm) of the PL band from these PQDs is 27 nm. $MAPbBr_3$ QDs containing the insulating capping ligands (3-aminopropyl)-triethoxysilane (APTES) and oleic acid (OA) as well as octylamine (OCTA) and OA were also synthesized according to the literature to compare with the BZA-BA-$MAPbBr_3$ QDs.[20,60] Panels b and c of Figure 1 correspond to the UV−vis absorption and PL spectra of the APTES-OA-$MAPbBr_3$ and OCTA-OA-$MAPbBr_3$ QDs, respectively. The APTES-OA-$MAPbBr_3$ QDs have a sharp exciton absorption peak at 520 nm and PL peak at 523 nm, while the OCTA-OA-$MAPbBr_3$ QDs have a much broader absorption band centered at 496 nm and PL peak at 514 nm. The fwhm of the PL band from APTES-OA-$MAPbBr_3$ QDs is 25 nm, while that of OCTA-OA-$MAPbBr_3$ QDs is 33 nm. The PLQY (vs fluorescein, 95%) values were calculated to be 46% and 71% for APTES-OA-$MAPbBr_3$ and OCTA-OA- $MAPbBr_3$ QDs, respectively, which are very similar to previously reported values.[20,56,60] In comparison, the PLQY values for the PQDs passivated with insulating ligands are lower than those of the PQDs with BZA/BA aromatic capping ligands, which is at 86%. We suggest that the difference in PLQY is less determined by the difference in the effect of spatial quantum confinement due to the different ligands or particle size and more related to the density of trap states of the PQDs that is critically influenced by the effectiveness of passivation by the ligands.

To determine the size and shape of the PQDs, transmission electron microscopy (TEM) measurements were conducted, with images shown in Figure 1d−f. The average diameter of the BZA-BA-$MAPbBr_3$, APTES-OA-$MAPbBr_3$, and OCTA-OA-$MAPbBr_3$ QDs are 6.3 ± 1.2, 6.8 ± 1.1, and 3.8 ± 0.9 nm, respectively. High-resolution TEM (HRTEM) was used to determine the lattice spacing of BZA-BA-$MAPbBr_3$ QDs. As shown in the lower left inset of Figure 1d, a lattice space of 0.28 nm was observed. This is an indication that the (002) crystal face of cubic $CH_3NH_3PbBr_3$ exists within the crystal lattice structure.[61] For further verification of the perovskite cubic phase presence, X-ray diffraction (XRD) was used to determine the QD crystal structure, as displayed in the upper left inset of Figure 1d. XRD peaks at 14.82°, 21.21°, 26.65°, 30.08°, 33.76°, 37.05°, 43.14°, 45.89°, 48.49°, 53.48°, 55.89°, and 58.24° indicate crystal planes assigned to the cubic phase of $MAPbBr_3$ perovskite, confirming its formation.[61]

To elucidate the organic surface layer of the PQDs, FTIR spectroscopy was employed to probe its capping ligand composition. For BZA-BA-$MAPbBr_3$ QDs, a weak peak at 3398 cm^{-1} is observed, indicating the presence of primary N−H stretching, as shown in Figure 2a. As presented in Figure 2b,c, stronger N−H stretching from BZA free ligand and $MAPbBr_3$ bulk occurs at 3291 and 3478 cm^{-1}, respectively. In the 3100−3000 cm^{-1} region, where aromatic C−H stretching occurs, three peaks at 3064, 3056, and 3028 cm^{-1} are observed for BZA-BA-$MAPbBr_3$ QDs, while three sharper peaks at 3085, 3065, and 3032 cm^{-1} are observed in BZA free ligand. This shift in aromatic C−H stretching from BZA free ligand to BZA-BA-$MAPbBr_3$ QDs provides evidence of ligand binding and change in vibrational modes from the unbound to bound states of the benzylamine molecule on the perovskite crystal lattice. Only one very strong and broad peak is observed for $MAPbBr_3$ bulk in this region, which corresponds to an ammonium salt. In addition, several aromatic C=C stretching and amine N−H bending peaks are expected to be in the range of 1700−1500 cm^{-1} for BZA-BA-$MAPbBr_3$ QDs, BZA free ligand, and $MAPbBr_3$ bulk; however, the region is too complex to distinguish. The most evident peaks for the presence of monosubstituted aromatic compounds are in the 770−730 and 720−680 cm^{-1} regions, where strong aromatic C−H bending

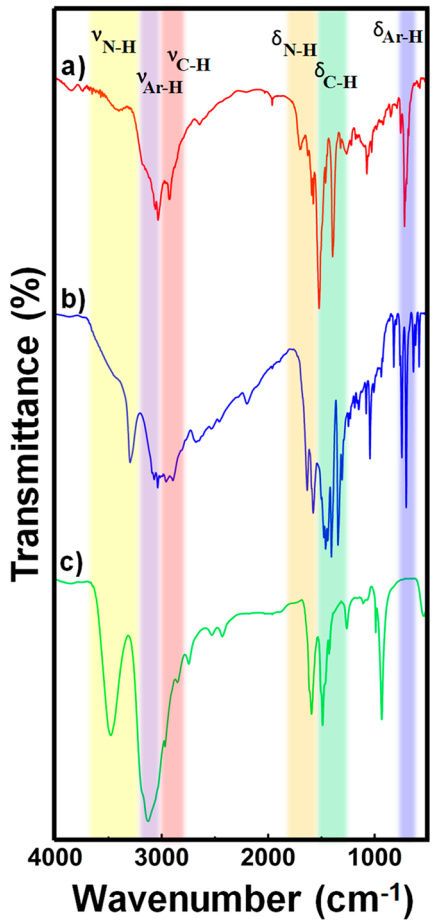

Figure 2. FT-IR spectra of (a) BZA-BA-$MAPbBr_3$ QDs, (b) BZA free ligand, and (c) $MAPbBr_3$ bulk.

DOI: 10.1021/acsenergylett.8b01754
ACS Energy Lett. 2018, 3, 2931−2939

peaks at 752 and 715 cm^{-1} are detected for BZA-BA-$MAPbBr_3$ QDs and peaks at 738 and 697 cm^{-1} are detected for BZA free ligand. Further detail in this region is illustrated in Figure S2. The $MAPbBr_3$ bulk contains no peaks in this region. In addition to the shift, as in the aromatic C−H stretching, the two aromatic C−H bending peaks are much broader in the BZA-BA-$MAPbBr_3$ QD FTIR spectra compared to BZA free ligand, which may reflect upon a change in vibrational modes, lifetime of vibrational states, and/or higher variety of vibrational modes from being bound in inhomogeneous positions on the $MAPbBr_3$ crystal lattice.

To investigate photogenerated charge carrier dynamics, time-correlated single-photon counting (TCSPC) was used to measure the fluorescence lifetime of the $MAPbBr_3$ QD solid film, as shown in Figure 3. Details of the measurement are described in the Supporting Information. The fluorescence decays were fitted using a double-exponential function:

$$L = A_1 \exp(-t/\tau_1) + A_2 \exp(-t/\tau_2) \quad (1)$$

The $MAPbBr_3$ QDs were casted into a solid film on insulating borosilicate glass as well as TiO_2 as a compact/mesoporous electron transporting material on conductive indium tin oxide (ITO) substrate to determine whether there is quenching of photogenerated free carriers due to charge collection. Depopulation of photogenerated carriers as a result of charge collection from the conductive substrate is elucidated in the observed change in rate and amplitude of the fast and slow decay components derived from the fitted double exponential function.[62−64] A shorter lifetime and larger amplitude of the fast component reflects effective extraction of photogenerated charge carriers. As shown in Figure 3a, the BZA-BA-$MAPbBr_3$ QD sample casted on the insulating borosilicate glass contains a fast decay component (τ_1) of 2.92 ns that contributes 48% to the total amplitude and a slow component (τ_2) of 21.9 ns with 52% contribution. While on the ITO-TiO_2 substrate, the fast component is 0.64 ns with 79% of the total amplitude and the slow component is 11.3 ns with a 21% total amplitude. The decrease in photogenerated charge carrier lifetime is indicative of more effective charge transfer and transport. For the APTES-OA-$MAPbBr_3$ QDs, as presented in Figure 3b, the fast decay component became slightly shorter from 1.24 ns on borosilicate to 0.77 ns on ITO-TiO_2 substrate, while the lifetime of the slow component remained almost the same. In addition, the fast component becomes more dominant in relative amplitude, which may indicate increased quenching or charge transport of photogenerated free carriers. The OCTA-OA-$MAPbBr_3$ QDs, as shown in Figure 3c, follows a similar trend observed in the APTES-OA-$MAPbBr_3$ QDs. The lifetime of the fast decay slightly decreased from 1.41 ns on borosilicate to 0.51 ns on ITO-TiO_2, while the longer lifetime did not change significantly. The following equation was used to calculate the average photogenerated charge carrier lifetime of the $MAPbBr_3$ QDs:

$$\langle\tau\rangle = \frac{A_1\tau_1^{\,2} + A_2\tau_2^{\,2}}{A_1\tau_1 + A_2\tau_2} \quad (2)$$

The average lifetime of the $MAPbBr_3$ QDs on conductive ITO-TiO_2 and insulating borosilicate glass was used to determine the electron-transfer rate constant (K_{et}) from the equation[65−67]

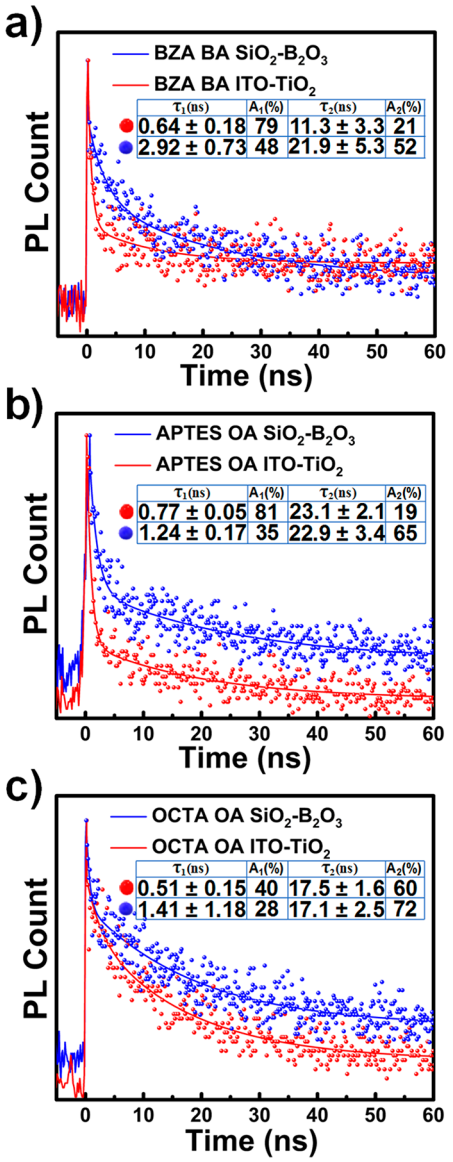

Figure 3. Time-resolved PL spectra of (a) BZA-BA-$MAPbBr_3$, (b) APTES-OA-$MAPbBr_3$, and (c) OCTA-OA-$MAPbBr_3$ QDs on SiO_2−B_2O_3 and ITO-TiO_2.

$$K_{et} = \frac{1}{\tau_{(PQD+TiO_2)}} - \frac{1}{\tau_{(PQD)}} \quad (3)$$

where $\tau_{(PQD+TiO_2)}$ and $\tau_{(PQD)}$ are the fluorescence decay on ITO-TiO_2 and borosilicate substrate, respectively. For BZA-BA-$MAPbBr_3$, APTES-OA-$MAPbBr_3$, and OCTA-OA-$MAPbBr_3$ QDs, the electron injection rate constants are calculated to be 55.7, 4.35, and 1.99 μs^{-1}, respectively. Accordingly, passivating $MAPbBr_3$ QDs with BZA and BA compared to APTES and OA as well as OCTA and OA has improved the electron injection rate by more than 6-fold and 2-fold, respectively.

For further characterization, the charge transport properties of the PQDs passivated with conductive aromatic ligands were examined by electrochemical impedance spectroscopy (EIS). The EIS measurements were carried out on fluorine-doped tin oxide (FTO) glass with films of $MAPbBr_3$ QDs and taken in the frequency range between 1 MHz and 0.1 Hz at open-circuit voltage. Further detail of the EIS measurement is found in the

DOI: 10.1021/acsenergylett.8b01754
ACS Energy Lett. 2018, 3, 2931−2939

Supporting Information. Figure 4a shows the Nyquist spectra of the different PQD films with the equivalent circuit in the

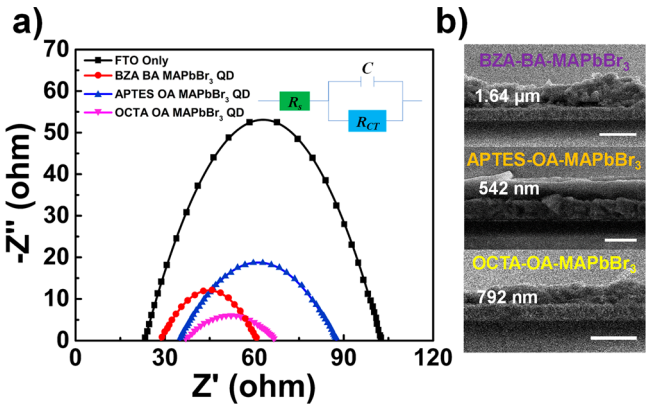

Figure 4. (a) Electrochemical impedance responses of FTO without film deposited and with BZA-BA-$MAPbBr_3$, APTES-OA-$MAPbBr_3$, and OCTA-OA-$MAPbBr_3$ QD film deposited. (b) Cross-sectional SEM images of the different QD film deposits used for EIS measurements. Scale bars represent 2, 1, and 1 μm, respectively.

inset, and Figure 4b displays the film thickness of each PQD used in EIS measurements. Increasing the thickness-to-surface area ratio will increase the impedance of the film.[68] Even with a thicker film (1.64 μm), BZA-BA-$MAPbBr_3$ QDs are observed to have a lower impedance compared to APTES-OA-$MAPbBr_3$ (542 nm) and OCTA-OA-$MAPbBr_3$ (792 nm) QD films. This supports the conclusion that the films composed of PQDs with conjugated ligands are more conductive. In the Nyquist spectra, the first intercept of the semicircle on the real axis from Figure 4a corresponds to the series resistance (R_s). Compared to the other two PQD solid films, APTES-OA-$MAPbBr_3$ and OCTA-OA-$MAPbBr_3$, with R_s values of 35.0 Ω and 36.8 Ω, respectively, the BZA-BA-$MAPbBr_3$ QD solid film has less series resistance with a R_s value of 28.6 Ω. The mechanism in the EIS measurement is reduction of PQD film from electron transport in the FTO working electrode; therefore, the R_s is highly dependent on the interaction between the PQD film and FTO substrate. The conductive aromatic capping ligands with sp^2 bond hybridization and electron delocalization allows sufficient electron cloud overlap with the PQD core, which can explain the lower series resistance compared to the other PQD films with insulating capping ligands. The second intercept in the Nyquist spectra represents the charge-transfer (R_{CT}) ability of the material, which is heavily dependent on the interaction of the electrolyte used in the measurement. Tetra-*n*-butylammonium hexafluorophosphate (Bu_4NPF_6) electrolyte was used in a similar spectroelectrochemical setup previously reported for PQDs.[69] This electrolyte contains hydrophobic butyl-alkyl groups that interact favorably with the hydrophobic ligands, such as OCTA, APTES, OA, BZA, and BA through London dispersion forces. In addition, the hydrophobic electrolyte disfavors the polar FTO glass. As a result, the charge transfer from the FTO to the electrolyte is a much slower process with a R_{CT} of 102 Ω. The BZA-BA-$MAPbBr_3$ QD film has not only the lowest R_s but also the lowest R_{CT} at 61.0 Ω, compared to APTES-OA-$MAPbBr_3$ QD film at 87.6 Ω and OCTA-OA-$MAPbBr_3$ QD film at 66.9 Ω. To qualitatively compare the BZA-BA-$MAPbBr_3$, APTES-OA-$MAPbBr_3$, and OCTA-OA-$MAPbBr_3$ QD films, the lifetime of the charge transfer was calculated to be 0.6, 4.4, and 3.2 ms, respectively.[70] In addition, the charge mobility (μ) was calculated using the above lifetimes and the diffusion length (L_d) of a previously reported $MAPbBr_3$ film,[71,72] which turn out to be 0.01197, 0.001640, and 0.002258 $cm^2\ V^{-1}\ s^{-1}$ for the three samples, respectively (details are in the Supporting Information). Overall, these measurements and calculations have provided evidence that the conductive aromatic ligands enhance the conductivity and charge transport of the QD film.

To substantiate PQD film reduction in the EIS measurements and examine the redox activity of the BZA-BA-$MAPbBr_3$, APTES-OA-$MAPbBr_3$, and OCTA-OA-$MAPbBr_3$ QD films, cyclic voltammetry (CV) measurements were conducted. As shown in Figure 5, only minor change in current density is observed with FTO substrate as the electrode compared to CV measurements with PQD film deposit. In addition, the positive and negative potential sweeps

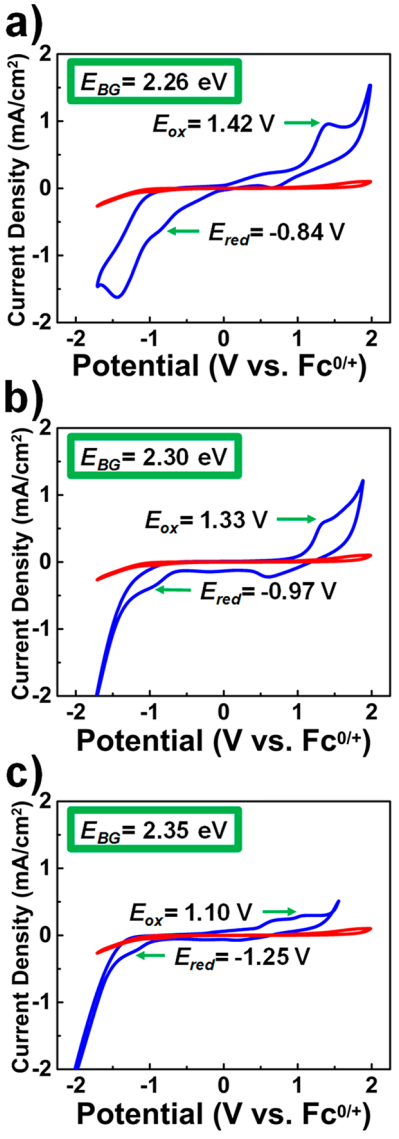

Figure 5. Cyclic voltammograms of (a) BZA-BA-$MAPbBr_3$, (b) APTES-OA-$MAPbBr_3$, and (c) OCTA-OA-$MAPbBr_3$ QD film. FTO electrode with QD film deposit is represented by the blue line, and FTO without QD film is in red.

DOI: 10.1021/acsenergylett.8b01754
ACS Energy Lett. 2018, 3, 2931−2939

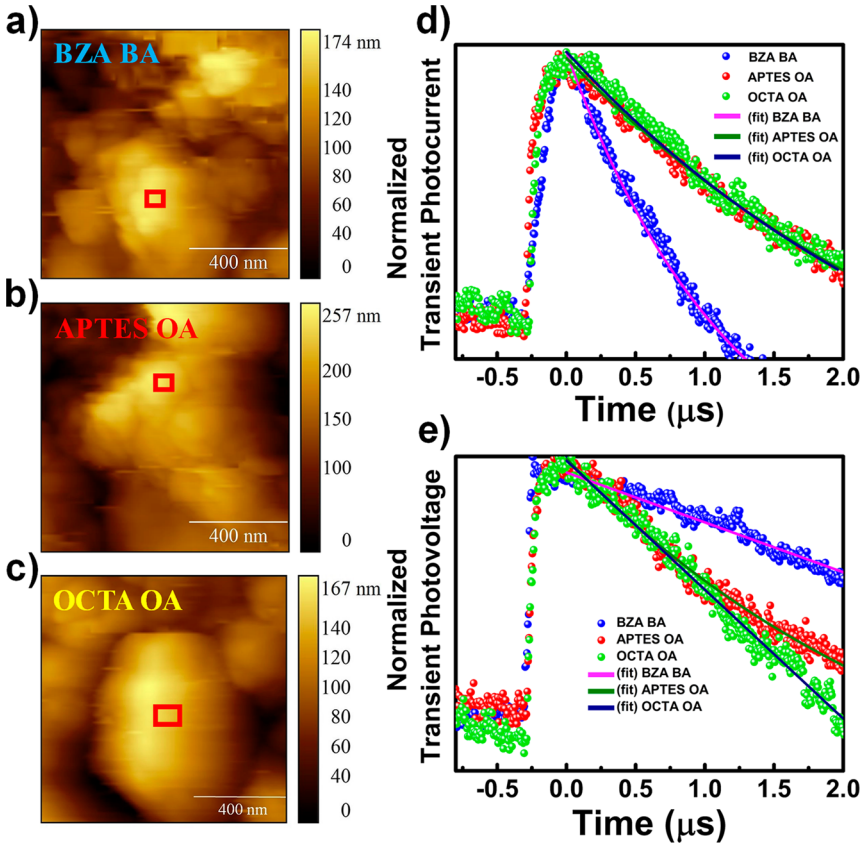

Figure 6. AFM topography images of (a) BZA-BA-MAPbBr$_3$, (b) APTES-OA-MAPbBr$_3$, and (c) OCTA-OA-MAPbBr$_3$ PQD films. Red squares indicate the areas measured. (d) Normalized TPC decay curve and (e) normalized TPV decay curve from the corresponding PQDs.

show the current density increases higher in BZA-BA-MAPbBr$_3$ QD film, as depicted in Figure 5a, compared to the APTES-OA-MAPbBr$_3$ and OCTA-OA-MAPbBr$_3$ QD films shown in panels b and c of Figure 5, respectively. When area under the curve, which is the power per active surface area of electrode, is compared, the BZA-BA-MAPbBr$_3$ QD film is 1.6 and 2.7 times higher than APTES-OA-MAPbBr$_3$ and OCTA-OA-MAPbBr$_3$ QD film, respectively.

From specific oxidation and reduction peaks in the CV diagram, bandgap energy values are calculated to be 2.26, 2.30, and 2.35 eV, for BZA-BA-MAPbBr$_3$, APTES-OA-MAPbBr$_3$, and OCTA-OA-MAPbBr$_3$ QD films, respectively. These values are in good agreement based on the bandgap energies calculated from the UV−vis absorption spectra (Figure S1), which are 2.25, 2.33, and 2.32 eV, respectively. Using the oxidation and reduction peaks corresponding to the band energies referenced to an internal standard (ferrocene/ferrocenium), the highest occupied molecular orbital (HOMO) and lowest unoccupied molecular orbital (LUMO) energy levels were calculated. For OCTA-OA-MAPbBr$_3$ QDs, the energy levels are −3.55 eV LUMO and −5.90 eV HOMO. For BZA-BA-MAPbBr$_3$ QDs, the LUMO energy level is lower at −3.96 eV as well as the HOMO energy level at −6.22 eV. This result could be due to an inductive effect, where the more electronegative sp^2 carbon atoms in the ligands are drawing more electron density away from the perovskite lattice, thus lowering the LUMO energy level. Furthermore, APTES-OA-MAPbBr$_3$ QDs may have the same effect as the APTES ligand has on electronegative oxygen atoms. The calculated HOMO energy level for these PQDs is −6.13 eV, and the LUMO is −3.83 eV. Considering the work function of the FTO substrate, which has been reported to be between −5.0 and −4.4 eV,[73] the BZA-BA-MAPbBr$_3$ QDs have a more favorable LUMO energy level for electron transport than OCTA-OA-MAPbBr$_3$ QDs. However, APTES-OA-MAPbBr$_3$ QDs have a LUMO very similar to that of BZA-BA-MAPbBr$_3$ QDs and yet still show a paralleled performance with OCTA-OA-MAPbBr$_3$ QDs in EIS and CV measurements. Therefore, it is concluded that the energy level alignment in the PQD films with the FTO substrate did not significantly impact these electrochemical measurements; however, to some extent, it favors BZA-BA-MAPbBr$_3$ and APTES-OA-MAPbBr$_3$ QDs over OCTA-OA-MAPbBr$_3$ QDs.

To provide further evidence of improved electrical properties from PQDs passivated with conductive aromatic ligands, local transient photocurrent (TPC) and transient photovoltage (TPV) decays were measured using conductive atomic force microscopy (AFM). Details of the TPC and TPV measurements are in the Supporting Information. As shown from the AFM topography images in Figure 6a−c, a 100 × 100 nm^2 area identified as the red square with similar film thickness was measured for BZA-BA-MAPbBr$_3$, APTES-OA-MAPbBr$_3$, and OCTA-OA-MAPbBr$_3$ QD solid film on FTO substrate. The charge transport time, recorded from TPC, corresponds directly to the conductivity and charge mobility of the material. TPC decay curves are displayed in Figure 6d. Charge transport lifetimes of 1.52, 2.15, and 1.97 μs were measured for BZA-BA-MAPbBr$_3$, APTES-OA-MAPbBr$_3$, and OCTA-OA-MAPbBr$_3$ QD films, respectively. Therefore, BZA-BA-MAPbBr$_3$ QDs outperform the PQDs with insulating capping ligands because charges are able to travel faster through the PQD layer between the two electrodes. To analyze the charge

DOI: 10.1021/acsenergylett.8b01754
ACS Energy Lett. 2018, 3, 2931−2939

recombination behavior of the PQD solid films, the charge carrier lifetime was measured by TPV. A longer charge carrier lifetime signifies a slower rate of recombination and therefore more efficient charge extraction. The TPV decay curves, as depicted in Figure 6e, translate to 2.92, 2.43, and 2.28 μs charge carrier lifetimes for BZA-BA-$MAPbBr_3$, APTES-OA-$MAPbBr_3$, and OCTA-OA-$MAPbBr_3$ QDs, respectively. BZA-BA-$MAPbBr_3$ QDs have not only a faster charge transport time but also a slower charge carrier lifetime, which is desired for device applications that rely on efficient charge transport and extraction.

In summary, we report the synthesis and characterization of $MAPbBr_3$ QDs surface-passivated with conductive aromatic capping ligands, benzylamine, and benzoic acid. The BZA-BA-$MAPbBr_3$ QDs are observed to have a high PLQY of 86%. In addition, compared to PQDs with insulating capping ligands, BZA-BA-$MAPbBr_3$ QDs demonstrated higher conductivity based on EIS and TPC measurements and longer charge carrier lifetime based on TPV measurements. Furthermore, using cyclic voltammetry, it is shown BZA-BA-$MAPbBr_3$ QD film generates much greater current density than APTES-OA-$MAPbBr_3$ and OCTA-OA-$MAPbBr_3$ QD film. The combination of high PLQY of the colloidal PQDs in solution, which usually correlates to lower trap density,[74−77] and improved electrical/electronic properties of the PQD film is desirable for potential optoelectronic device applications.

■ ASSOCIATED CONTENT

Supporting Information

The Supporting Information is available free of charge on the ACS Publications website at DOI: 10.1021/acsenergylett.8b01754.

Experimental section, additional FTIR characterization, PQD film absorption/PL spectra, and time-resolved PL spectra (PDF)

■ AUTHOR INFORMATION

Corresponding Author

*E-mail: zhang@ucsc.edu.

ORCID

Sarah Lindley: 0000-0002-6600-0412
Qiquan Qiao: 0000-0002-4555-7887
Jin Z. Zhang: 0000-0003-3437-912X

Notes

The authors declare no competing financial interest.

■ ACKNOWLEDGMENTS

This research was supported by NASA through MACES (NNX15AQ01A) and a UCSC Committee on Research Special Research Grant. Work at the Molecular Foundry was supported by the Office of Science, Office of Basic Energy Sciences, of the U.S. Department of Energy under Contract DE-AC02-05CH11231. Q.Q. acknowledges the financial support from NSF MRI (1428992), NASA EPSCoR (NNX15AM83A), and US-Egypt Science and Technology (S&T) Joint Fund. This work is made possible by the generous support of the American people through the United States Agency for International Development (USAID). The contents are the responsibility of the recipient and do not necessarily reflect the views of USAID or the United States Government.

■ REFERENCES

(1) Kamat, P. V. Meeting the Clean Energy Demand: Nanostructure Architectures for Solar Energy Conversion. *J. Phys. Chem. C* **2007**, *111*, 2834−2860.
(2) Kamat, P. V. Quantum Dot Solar Cells. Semiconductor Nanocrystals as Light Harvesters. *J. Phys. Chem. C* **2008**, *112*, 18737−18753.
(3) Kamat, P. V. Quantum Dot Solar Cells. The *Next Big Thing* in Photovoltaics. *J. Phys. Chem. Lett.* **2013**, *4*, 908−918.
(4) Kagan, C. R.; Murray, C. B. Charge Transport in Strongly Coupled Quantum Dot Solids. *Nat. Nanotechnol.* **2015**, *10*, 1013−1026.
(5) Carey, G. H.; Abdelhady, A. L.; Ning, Z.; Thon, S. M.; Bakr, O. M.; Sargent, E. H. Colloidal Quantum Dot Solar Cells. *Chem. Rev.* **2015**, *115*, 12732−12763.
(6) Sogabe, T.; Shen, Q.; Yamaguchi, K. Recent Progress on Quantum Dot Solar Cells: A Review. *J. Photonics Energy* **2016**, *6*, 040901.
(7) Voznyy, O. V.; Sutherland, B. R.; Ip, A. H.; Zhitomirsky, D.; Sargent, E. H. Engineering Charge Transport by Heterostructuring Solution-processed Semiconductors. *Nat. Rev. Mater.* **2017**, *2*, 17026.
(8) Luo, B.; Bonabi Naghadeh, S.; Zhang, J. Z. Lead Halide Perovskite Nanocrystals: Stability, Surface Passivation, and Structural Control. *ChemNanoMat* **2017**, *3*, 456−465.
(9) Bonabi Naghadeh, S.; Luo, B.; Abdelmageed, G.; Pu, Y.-C.; Zhang, C.; Zhang, J. Z. Photophysical Properties and Improved Stability of Organic−Inorganic Perovskite by Surface Passivation. *J. Phys. Chem. C* **2018**, *122*, 15799−15818.
(10) Brus, L. E. Electron−electron and Electron-hole Interactions in Small Semiconductor Crystallites: The Size Dependence of the Lowest Excited Electronic State. *J. Chem. Phys.* **1984**, *80*, 4403−4409.
(11) Ekimov, A. I.; Efros, A. L.; Onushchenko, A. A. Quantum Size Effect in Semiconductor Microcrystals. *Solid State Commun.* **1985**, *56*, 921−924.
(12) Weller, H. Quantized Semiconductor Particles: A Novel State of Matter for Materials Science. *Adv. Mater.* **1993**, *5*, 88−95.
(13) Aristidou, N.; Sanchez-Molina, I.; Chotchuangchutchaval, T.; Brown, M.; Martinez, L.; Rath, T.; Haque, S. A. The Role of Oxygen in the Degradation of Methylammonium Lead Trihalide Perovskite Photoactive Layers. *Angew. Chem., Int. Ed.* **2015**, *54*, 8208−8212.
(14) Mosconi, E.; Azpiroz, J. M.; De Angelis, F. *Ab Initio* Molecular Dynamics Simulations of Methylammonium Lead Iodide Perovskite Degradation by Water. *Chem. Mater.* **2015**, *27*, 4885−4892.
(15) Christians, J. A.; Miranda Herrera, P. A.; Kamat, P. V. Transformation of the Excited State and Photovoltaic Efficiency of $CH_3NH_3PbI_3$ Perovskite upon Controlled Exposure to Humidified Air. *J. Am. Chem. Soc.* **2015**, *137*, 1530−1538.
(16) Yang, J.; Siempelkamp, B. D.; Mosconi, E.; De Angelis, F.; Kelly, T. L. Origin of the Thermal Instability in $CH_3NH_3PbI_3$ Thin Films Deposited on ZnO. *Chem. Mater.* **2015**, *27*, 4229−4236.
(17) Niu, G.; Guo, X.; Wang, L. Review of Recent Progress in Chemical Stability of Perovskite Solar Cells. *J. Mater. Chem. A* **2015**, *3*, 8970−8980.
(18) Zhao, J.; Cai, B.; Luo, Z.; Dong, Y.; Zhang, Y.; Xu, H.; Hong, B.; Yang, Y.; Li, L.; Zhang, W.; et al. Investigation of the Hydrolysis of Perovskite Organometallic Halide $CH_3NH_3PbI_3$ in Humidity Environment. *Sci. Rep.* **2016**, *6*, 21976.
(19) Abdelmageed, G.; Jewell, L.; Hellier, K.; Seymour, L.; Luo, B.; Bridges, F.; Zhang, J. Z.; Carter, S. Mechanisms for Light Induced Degradation in $MAPbI_3$ Perovskite Thin Films and Solar Cells. *Appl. Phys. Lett.* **2016**, *109*, 233905.
(20) Luo, B.; Pu, Y. C.; Lindley, S. A.; Yang, Y.; Lu, L.; Li, Y.; Li, X.; Zhang, J. Z. Organolead Halide Perovskite Nanocrystals: Branched Capping Ligands Control Crystal Size and Stability. *Angew. Chem., Int. Ed.* **2016**, *55*, 8864−8868.
(21) Marinova, N.; Franckevičius, M.; Matulaitienė, I.; Devižis, A.; Niaura, G.; Gulbinas, V.; Delgado, J. L. Hindered Amine Light Stabilizers Increase the Stability of Methylammonium Lead Iodide

DOI: 10.1021/acsenergylett.8b01754
ACS Energy Lett. 2018, 3, 2931−2939

Perovskite against Light and Oxygen. *ChemSusChem* **2017**, *10*, 3760−3764.
(22) Abdelmageed, G.; Mackeen, C.; Hellier, K.; Jewell, L.; Seymour, L.; Tingwald, M.; Bridges, F.; Zhang, J. Z.; Carter, S. Effect of Temperature on Light Induced Degradation in Methylammonium Lead Iodide Perovskite Thin Films and Solar Cells. *Sol. Energy Mater. Sol. Cells* **2018**, *174*, 566−571.
(23) Hines, D. A.; Kamat, P. V. Recent Advances in Quantum Dot Surface Chemistry. *ACS Appl. Mater. Interfaces* **2014**, *6*, 3041−3057.
(24) Pan, J.; Sarmah, S. P.; Murali, B.; Dursun, I.; Peng, W.; Parida, M. R.; Liu, J.; Sinatra, L.; Alyami, N.; Zhao, C.; et al. Air-Stable Surface-Passivated Perovskite Quantum Dots for Ultra-Robust, Single- and Two-Photon-Induced Amplified Spontaneous Emission. *J. Phys. Chem. Lett.* **2015**, *6*, 5027−5033.
(25) Huang, S.; Li, Z.; Kong, L.; Zhu, N.; Shan, A.; Li, L. Enhancing the Stability of $CH_3NH_3PbBr_3$ Quantum Dots by Embedding in Silica Spheres Derived from Tetramethyl Orthosilicate in "Waterless" Toluene. *J. Am. Chem. Soc.* **2016**, *138*, 5749−5752.
(26) Veldhuis, S. A.; Tay, Y. K. E.; Bruno, A.; Dintakurti, S. S. H.; Bhaumik, S.; Muduli, S. K.; Li, M.; Mathews, N.; Sum, T. C.; Mhaisalkar, S. G. Benzyl Alcohol-Treated $CH_3NH_3PbBr_3$ Nanocrystals Exhibiting High Luminescence, Stability, and Ultralow Amplified Spontaneous Emission Thresholds. *Nano Lett.* **2017**, *17*, 7424−7432.
(27) Abdelmageed, G.; Sully, H. R.; Bonabi Naghadeh, S.; El-Hag Ali, A.; Carter, S. A.; Zhang, J. Z. Improved Stability of Organometal Halide Perovskite Films and Solar Cells toward Humidity via Surface Passivation with Oleic Acid. *ACS Appl. Energy Mater.* **2018**, *1*, 387−392.
(28) Tan, Y.; Zou, Y.; Wu, L.; Huang, Q.; Yang, D.; Chen, M.; Ban, M.; Wu, C.; Wu, T.; Bai, S.; et al. Highly Luminescent and Stable Perovskite Nanocrystals with Octylphosphonic Acid as a Ligand for Efficient Light-Emitting Diodes. *ACS Appl. Mater. Interfaces* **2018**, *10*, 3784−3792.
(29) Krieg, F.; Ochsenbein, S. T.; Yakunin, S.; ten Brinck, S.; Aellen, P.; Süess, A.; Clerc, B.; Guggisberg, D.; Nazarenko, O.; Shynkarenko, Y.; et al. Colloidal $CsPbX_3$ (X = Cl, Br, I) Nanocrystals 2.0: Zwitterionic Capping Ligands for Improved Durability and Stability. *ACS Energy Lett.* **2018**, *3*, 641−646.
(30) Kovalenko, M. V.; Scheele, M.; Talapin, D. V. Colloidal Nanocrystals with Molecular Metal Chalcogenide Surface Ligands. *Science* **2009**, *324*, 1417−1420.
(31) Liu, D.; Gangishetty, M. K.; Kelly, T. L. Effect of $CH_3NH_3PbI_3$ Thickness on Device Efficiency in Planar Heterojunction Perovskite Solar Cells. *J. Mater. Chem. A* **2014**, *2*, 19873−19881.
(32) Lan, X.; Voznyy, O.; García de Arquer, F. P.; Liu, M.; Xu, J.; Proppe, A. H.; Walters, G.; Fan, F.; Tan, H.; Liu, M.; et al. 10.6% Certified Colloidal Quantum Dot Solar Cells via Solvent-Polarity-Engineered Halide Passivation. *Nano Lett.* **2016**, *16*, 4630−4634.
(33) Yang, Z.; Fan, J. Z.; Proppe, A. H.; García de Arquer, F. P.; Rossouw, D.; Voznyy, O.; Lan, X.; Liu, M.; Walters, G.; Quintero-Bermudez, R.; et al. Mixed-quantum-dot Solar Cells. *Nat. Commun.* **2017**, *8*, 1325.
(34) Karani, A.; Yang, L.; Bai, S.; Futscher, M. H.; Snaith, H. J.; Ehrler, B.; Greenham, N. C.; Di, D. Perovskite/Colloidal Quantum Dot Tandem Solar Cells: Theoretical Modeling and Monolithic Structure. *ACS Energy Lett.* **2018**, *3*, 869−874.
(35) Zhang, X.; Zhang, J.; Phuyal, D.; Du, J.; Tian, L.; Öberg, V. A.; Johansson, M. B.; Cappel, U. B.; Karis, O.; Liu, J.; et al. Inorganic $CsPbI_3$ Perovskite Coating on PbS Quantum Dot for Highly Efficient and Stable Infrared Light Converting Solar Cells. *Adv. Energy Mater.* **2018**, *8*, 1702049.
(36) Dibbell, R. S.; Youker, D. G.; Watson, D. F. Excited-State Electron Transfer from CdS Quantum Dots to TiO_2 Nanoparticles via Molecular Linkers with Phenylene Bridges. *J. Phys. Chem. C* **2009**, *113*, 18643−18651.
(37) Zillner, E.; Fengler, S.; Niyamakom, P.; Rauscher, F.; Köhler, K.; Dittrich, T. Role of Ligand Exchange at CdSe Quantum Dot Layers for Charge Separation. *J. Phys. Chem. C* **2012**, *116*, 16747−16754.
(38) Dugay, J.; Tan, P.; Ibrahim, M.; Garcia, J. C.; Lacroix, L.-M.; Fazzini, P.-F.; Viau, G.; Respaud, M. Charge Transport and Interdot Coupling Tuned by the Tunnel Barrier Length in Assemblies of Nanoparticles Surrounded by Organic Ligands. *Phys. Rev. B: Condens. Matter Mater. Phys.* **2014**, *89*, 041406.
(39) Chistyakov, A. A.; Zvaigzne, M. A.; Nikitenko, V. R.; Tameev, A. R.; Martynov, I. L.; Prezhdo, O. V. Optoelectronic Properties of Semiconductor Quantum Dot Solids for Photovoltaic Applications. *J. Phys. Chem. Lett.* **2017**, *8*, 4129−4139.
(40) Hoffman, J. B.; Alam, R.; Kamat, P. V. Why Surface Chemistry Matters for QD−QD Resonance Energy Transfer. *ACS Energy Lett.* **2017**, *2*, 391−396.
(41) Jeong, K. S.; Tang, J.; Liu, H.; Kim, J.; Schaefer, A. W.; Kemp, K.; Levina, L.; Wang, X.; Hoogland, S.; Debnath, R.; et al. Enhanced Mobility-Lifetime Products in PbS Colloidal Quantum Dot Photovoltaics. *ACS Nano* **2012**, *6*, 89−99.
(42) Chang, L. Y.; Lunt, R. R.; Brown, P. R.; Bulovic, V.; Bawendi, M. G. Low-Temperature Solution-Processed Solar Cells Based on PbS Colloidal Quantum Dot/CdS Heterojunctions. *Nano Lett.* **2013**, *13*, 994−999.
(43) Dai, M.-Q.; Yung, L.-Y. L. Ethylenediamine-Assisted Ligand Exchange and Phase Transfer of Oleophilic Quantum Dots: Stripping of Original Ligands and Preservation of Photoluminescence. *Chem. Mater.* **2013**, *25*, 2193−2201.
(44) Hines, D. A.; Kamat, P. V. Quantum Dot Surface Chemistry: Ligand Effects and Electron Transfer Reactions. *J. Phys. Chem. C* **2013**, *117*, 14418−14426.
(45) Crisp, R. W.; Kroupa, D. M.; Marshall, A. R.; Miller, E. M.; Zhang, J.; Beard, M. C.; Luther, J. M. Metal Halide Solid-state Surface Treatment for High Efficiency PbS and PbSe QD Solar Cells. *Sci. Rep.* **2015**, *5*, 9945.
(46) Cohen, E.; Gdor, I.; Romero, E.; Yochelis, S.; van Grondelle, R.; Paltiel, Y. Achieving Exciton Delocalization in Quantum Dot Aggregates Using Organic Linker Molecules. *J. Phys. Chem. Lett.* **2017**, *8*, 1014−1018.
(47) Wheeler, L. M.; Sanehira, E. M.; Marshall, A. R.; Schulz, P.; Suri, M.; Anderson, N. C.; Christians, J. A.; Nordlund, D.; Sokaras, D.; Kroll, T.; et al. Targeted Ligand-Exchange Chemistry on Cesium Lead Halide Perovskite Quantum Dots for High-Efficiency Photovoltaics. *J. Am. Chem. Soc.* **2018**, *140*, 10504−10513.
(48) Sharma, S. N.; Pillai, Z. S.; Kamat, P. V. Photoinduced Charge Transfer between CdSe Quantum Dots and *p*-Phenylenediamine. *J. Phys. Chem. B* **2003**, *107*, 10088−10093.
(49) Liu, I.-S.; Lo, H.-H.; Chien, C.-T.; Lin, Y.-Y.; Chen, C.-W.; Chen, Y.-F.; Su, W.-F.; Liou, S.-C. Enhancing Photoluminescence Quenching and Photoelectric Properties of CdSe Quantum Dots with Hole Accepting Ligands. *J. Mater. Chem.* **2008**, *18*, 675−682.
(50) Knowles, K. E.; Tice, D. B.; McArthur, E. A.; Solomon, G. C.; Weiss, E. A. Chemical Control of the Photoluminescence of CdSe Quantum Dot−Organic Complexes with a Series of Para-Substituted Aniline Ligands. *J. Am. Chem. Soc.* **2010**, *132*, 1041−1050.
(51) Donakowski, M. D.; Godbe, J. M.; Sknepnek, R.; Knowles, K. E.; Olvera de la Cruz, M.; Weiss, E. A. A Quantitative Description of the Binding Equilibria of para-Substituted Aniline Ligands and CdSe Quantum Dots. *J. Phys. Chem. C* **2010**, *114*, 22526−22534.
(52) Tan, Y.; Jin, S.; Hamers, R. J. Influence of Hole-Sequestering Ligands on the Photostability of CdSe Quantum Dots. *J. Phys. Chem. C* **2013**, *117*, 313−320.
(53) Frederick, M. T.; Amin, V. A.; Swenson, N. K.; Ho, A. Y.; Weiss, E. A. Control of Exciton Confinement in Quantum Dot−Organic Complexes through Energetic Alignment of Interfacial Orbitals. *Nano Lett.* **2013**, *13*, 287−292.
(54) Zuo, L.; Chen, Q.; De Marco, N.; Hsieh, Y.-T.; Chen, H.; Sun, P.; Chang, S.-Y.; Zhao, H.; Dong, S.; Yang, Y. Tailoring the Interfacial Chemical Interaction for High-Efficiency Perovskite Solar Cells. *Nano Lett.* **2017**, *17*, 269−275.
(55) Pu, Y.-C.; Ma, H.; Sajben, N.; Xia, G.; Zhang, J.; Li, Y.; Zhang, J. Z. Dependence of Interfacial Charge Transfer on Bifunctional

DOI: 10.1021/acsenergylett.8b01754
ACS Energy Lett. 2018, 3, 2931−2939

Aromatic Molecular Linkers in CdSe Quantum Dot Sensitized TiO_2 Photoelectrodes. *ACS Appl. Energy Mater.* **2018**, *1*, 2907−2917.
(56) Dai, J.; Xi, J.; Li, L.; Zhao, J.; Shi, Y.; Zhang, W.; Ran, C.; Jiao, B.; Hou, X.; Duan, X.; et al. Charge Transport between Coupling Colloidal Perovskite Quantum Dots Assisted by Functional Conjugated Ligands. *Angew. Chem., Int. Ed.* **2018**, *57*, 5754−5758.
(57) Wang, F.; Geng, W.; Zhou, Y.; Fang, H.-H.; Tong, C.-J.; Loi, M. A.; Liu, L.-M. Phenylalkylamine Passivation of Organolead Halide Perovskites Enabling High-Efficiency and Air-Stable Photovoltaic Cells. *Adv. Mater.* **2016**, *28*, 9986−9992.
(58) Zhou, Y.; Wang, F.; Cao, Y.; Wang, J.-P.; Fang, H.-H.; Loi, M. A.; Zhao, N.; Wong, C.-P. Benzylamine-Treated Wide-Bandgap Perovskite with High Thermal-Photostability and Photovoltaic Performance. *Adv. Energy Mater.* **2017**, *7*, 1701048.
(59) Luo, B.; Bonabi Naghadeh, S.; Allen, A.; Li, X.; Zhang, J. Z. Peptide-Passivated Lead Halide Perovskite Nanocrystals Based on Synergistic Effect between Amino and Carboxylic Functional Groups. *Adv. Funct. Mater.* **2017**, *27*, 1604018.
(60) Zhang, F.; Zhong, H.; Chen, C.; Wu, X.; Hu, X.; Huang, X.; Han, X.; Zou, B.; Dong, Y. Brightly Luminescent and Color-Tunable Colloidal $CH_3NH_3PbX_3$ (X = Br, I, Cl) Quantum Dots: Potential Alternatives for Display Technology. *ACS Nano* **2015**, *9*, 4533−4542.
(61) Schmidt, L. C.; Pertegas, A.; Gonzalez-Carrero, S.; Malinkiewicz, O.; Agouram, S.; Minguez Espallargas, G.; Bolink, H. J.; Galian, R. E.; Perez-Prieto, J. Nontemplate Synthesis of $CH_3NH_3PbBr_3$ Perovskite Nanoparticles. *J. Am. Chem. Soc.* **2014**, *136*, 850−853.
(62) Yeo, J. S.; Kang, R.; Lee, S.; Jeon, Y. J.; Myoung, N.; Lee, C. L.; Kim, D. Y.; Yun, J. M.; Seo, Y. H.; Kim, S. S.; et al. Highly Efficient and Stable Planar Perovskite Solar Cells with Reduced Graphene Oxide Nanosheets as Electrode Interlayer. *Nano Energy* **2015**, *12*, 96−104.
(63) Liang, P. W.; Liao, C. Y.; Chueh, C. C.; Zuo, F.; Williams, S. T.; Xin, X. K.; Lin, J.; Jen, A. K. Additive Enhanced Crystallization of Solution − Processed Perovskite for Highly Efficient Planar − Heterojunction Solar Cells. *Adv. Mater.* **2014**, *26*, 3748−3754.
(64) Li, H.; Tao, L.; Huang, F.; Sun, Q.; Zhao, X.; Han, J.; Shen, Y.; Wang, M. Enhancing Efficiency of Perovskite Solar Cells via Surface Passivation with Graphene Oxide Interlayer. *ACS Appl. Mater. Interfaces* **2017**, *9*, 38967−38976.
(65) Ning, Z.; Tian, H.; Qin, H.; Zhang, Q.; Ågren, H.; Sun, L.; Fu, Y. Wave-Function Engineering of CdSe/CdS Core/Shell Quantum Dots for Enhanced Electron Transfer to a TiO_2 Substrate. *J. Phys. Chem. C* **2010**, *114*, 15184−15189.
(66) Kongkanand, A.; Tvrdy, K.; Takechi, K.; Kuno, M.; Kamat, P. V. Quantum Dot Solar Cells. Tuning Photoresponse through Size and Shape Control of CdSe-TiO_2 Architecture. *J. Am. Chem. Soc.* **2008**, *130*, 4007−4015.
(67) Jamshidi, A.; Yuan, C.; Chmyrov, V.; Widengren, J.; Sun, L.; Ågren, H. Efficiency Enhanced Collodial Mn-Doped Type II Core/Shell ZnSe/CdS Quantum Dot Sensitized Hybrid Solar Cells. *J. Nanomater.* **2015**, *2015*, 921903.
(68) Saif, A. A.; Poopalan, P. Effect of the Film Thickness on the Impedance Behavior of Sol-Gel $Ba_{0.6}Sr_{0.4}TiO_3$ Thin Films. *Phys. B* **2011**, *406*, 1283−1288.
(69) Samu, G. F.; Scheidt, R. A.; Kamat, P. V.; Janáky, C. Electrochemistry and Spectroelectrochemistry of Lead Halide Perovskite Films: Materials Science Aspects and Boundary Conditions. *Chem. Mater.* **2018**, *30*, 561−569.
(70) Kim, Y. C.; Kim, K. H.; Son, D.-Y.; Jeong, D.-N.; Seo, J.-Y.; Choi, Y. S.; Han, I. T.; Lee, S. Y.; Park, N. G. Printable Organometallic Perovskite Enables Large-area, Low-dose X-ray Imaging. *Nature* **2017**, *550*, 87−91.
(71) Zhumekenov, A. A.; Saidaminov, M. I.; Haque, M. A.; Alarousu, E.; Sarmah, S. P.; Murali, B.; Dursun, I. D.; Miao, X.-H.; Abdelhady, A. L.; Wu, T.; et al. Formamidinium Lead Halide Perovskite Crystals with Unprecedented Long Carrier Dynamics and Diffusion Length. *ACS Energy Lett.* **2016**, *1*, 32−37.
(72) Hodes, G.; Kamat, P. V. Understanding the Implication of Carrier Diffusion Length in Photovoltaic Cells. *J. Phys. Chem. Lett.* **2015**, *6*, 4090−4092.
(73) Helander, M. G.; Greiner, M. T.; Wang, Z. B.; Tang, W. M. Work Function of Fluorine Doped Tin Oxide. *J. Vac. Sci. Technol., A* **2011**, *29*, 011019.
(74) Miller, O. D.; Yablonovitch, E.; Kurtz, S. R. Strong Internal and External Luminescence as Solar Cells Approach the Shockley−Queisser Limit. *IEEE J. Photovoltaics* **2012**, *2*, 303−311.
(75) Saidaminov, M. I.; Almutlaq, J.; Sarmah, S.; Dursun, I.; Zhumekenov, A. A.; Begum, R.; Pan, J.; Cho, N.; Mohammed, O. F.; Bakr, O. M. Pure Cs_4PbBr_6: Highly Luminescent Zero-Dimensional Perovskite Solids. *ACS Energy Lett.* **2016**, *1*, 840−845.
(76) Sutter-Fella, C. M.; Li, Y.; Amani, M.; Ager, J. W.; Toma, F. M.; Yablonovitch, E.; Sharp, I. D.; Javey, A. High Photoluminescence Quantum Yield in Band Gap Tunable Bromide Containing Mixed Halide Perovskites. *Nano Lett.* **2016**, *16*, 800−806.
(77) Braly, I. L.; deQuilettes, D. W.; Pazos-Outón, L. M.; Burke, S.; Ziffer, M. E.; Ginger, D. S.; Hillhouse, H. W. Hybrid Perovskite Films Approaching the Radiative Limit with over 90% Photoluminescence Quantum Efficiency. *Nat. Photonics* **2018**, *12*, 355−361.

NOTE ADDED AFTER ASAP PUBLICATION

This article published November 14, 2018 with incorrect values for the electron injection rate constants. The correct values published November 19, 2018.

DOI: 10.1021/acsenergylett.8b01754
ACS Energy Lett. 2018, 3, 2931−2939